Electrohydrodynamic drift of a drop away from an insulating wall

Diptendu Sen [1,*] Mohammadhossein Firouznia [2,3,*] Jeremy A. Koch [4]
David Saintillan [2] and Petia M. Vlahovska [4]
[1] *Department of Mechanical Engineering, Northwestern University, Evanston, Illinois 60208, USA*
[2] *Department of Mechanical and Aerospace Engineering, University of California, San Diego, 9500 Gilman Drive, La Jolla, California 92093, USA*
[3] *Center for Computational Biology, Flatiron Institute, New York, New York 10010, USA*
[4] *Department of Engineering Sciences and Applied Mathematics, Northwestern University, Evanston, Illinois 60208, USA*

(Received 24 December 2024; accepted 2 June 2025; published 1 July 2025)

An isolated charge-neutral drop suspended in an unbounded medium does not migrate in a uniform dc electric field. A nearby wall breaks the symmetry and causes the drop to drift towards or away from the boundary, depending on the electric properties of the fluids and the wall. In the case of an electrically insulating wall and an electric field applied tangentially to the wall, the interaction of the drop with its electrostatic image gives rise to repulsion by the wall. However, the electrohydrodynamic flow causes either repulsion for a drop with $R/P < 1$, where R and P are the drop-to-medium ratios of conductivity and permittivity, respectively, or attraction for $R/P > 1$. We experimentally measure droplet trajectories and quantify the wall-induced electrohydrodynamic lift in the case $R/P < 1$. Numerical simulations using the boundary integral method agree well with the experiment and also explore the $R/P > 1$ case. The results show that the lateral migration of a drop in a uniform electric field applied parallel to an insulating wall is dominated by the long-range flow due to the image stresslet.

DOI: 10.1103/l8pb-9qxk

I. INTRODUCTION

Electric fields are widely used to manipulate particles such as colloids [1–4], droplets [5,6], cells and cellular mimetics [7–9] or to assess properties of biomimetic membranes [10,11]. In many of these applications, the particles are close to boundaries. In an applied uniform electric field, even a charge-free particle can drift due to the interaction of the particle induced dipole and its image [12–16]. This dielectrophoretic (DEP) interaction is attractive with an electrode, and repulsive with an insulating wall. In the far field, the induced migration velocity decreases with the inverse fourth power of the distance to the boundary.

Electrohydrodynamic (EHD) flows induce interaction that is longer-ranged compared to the DEP one, decaying in the far field as the inverse second power of the distance to the boundary. To understand this interaction, it is useful to consider an analogy with the induced-charge electro-osmotic (ICEO) flow around a polarizable particle, where fluid is drawn along the field axis and expelled radially in the equatorial plane. Near a wall, this flow pumps fluid into the gap between the particle and the wall, creating an effective repulsion [14,17]. The flow around a droplet in a uniform electric field exhibits a pattern similar to the ICEO [18] and thus a drop is expected to migrate relative to a nearby wall. However, unlike an ideally polarizable particle, the direction of droplet migration

*These authors contributed equally to this work.

depends on the electric properties of the droplet and suspending fluid. The electrohydrodynamic flow is driven by electric shear stresses due to induced surface charges [18,19]. For a drop in an unbounded medium and subjected to a uniform electric field, the resulting flow is axisymmetric about the applied field direction. In the case of a spherical drop, the interfacial velocity is

$$\boldsymbol{u}(r = a, \theta, \phi) = \beta_T \sin 2\theta\, \hat{\theta}, \tag{1}$$

where (r, θ, ϕ) are the spherical coordinates, with θ being the angle away from the applied field direction, $\boldsymbol{E}_0 = E_0\hat{\mathbf{z}}$, and

$$\beta_T = \frac{9\varepsilon E_0^2 a}{10\mu}\frac{\mathrm{R} - \mathrm{P}}{(1 + \lambda)(\mathrm{R} + 2)^2}, \tag{2}$$

a is the drop radius, and $\lambda = \mu_d/\mu$ is the viscosity ratio between the drop and suspending fluid. The direction of the surface flow is determined by the difference of the conductivity ratio ($\mathrm{R} = \sigma_d/\sigma$) and the permittivity ratio ($\mathrm{P} = \varepsilon_d/\varepsilon$) between the drop and the suspending fluid. If $\mathrm{R}/\mathrm{P} < 1$, the surface flow is from pole to equator, i.e., the fluid is drawn in at the poles and pushed away from the drop at the equator. The flow direction is reversed for $\mathrm{R}/\mathrm{P} > 1$. Accordingly, by analogy with the ICEO effect on a particle near an insulating wall, the EHD flow is expected to repel a droplet with $\mathrm{R}/\mathrm{P} < 1$ and attract one with $\mathrm{R}/\mathrm{P} > 1$.

To estimate the droplet migration velocity, we consider the far field of the unbounded EHD flow, which is a stresslet flow,

$$\boldsymbol{u}(\boldsymbol{r}) = \beta_T(-1 + 3\cos^2\theta)\frac{a^2}{r^2}\hat{\boldsymbol{r}}. \tag{3}$$

To satisfy the boundary conditions at the wall, a reflection to this velocity is introduced. Thus, for a droplet far from the plane, the leading order droplet migration velocity is that of the flow velocity of the stresslet image system evaluated at the position of the droplet; in particular, the drop migration velocity U_{EHD} normal to a rigid wall due to the electrohydrodynamic flow is proportional to the stresslet component S_{nn} in the direction of the plane unit normal [20],

$$U_{\mathrm{EHD}} = -\frac{9S_{nn}}{64\pi\mu h^2}, \tag{4}$$

where h is the distance from the droplet center to the wall. In the configuration described in Fig. 2, $S_{nn} = 8\pi\mu\beta_T a^2/3$ and the corresponding migration velocity is

$$U_{\mathrm{EHD}} = -\frac{1}{h^2}\left(\frac{\varepsilon E_0^2 a^3}{\mu}\right)\left[\frac{27(\mathrm{R} - \mathrm{P})}{80(1 + \lambda)(2 + \mathrm{R})^2}\right]. \tag{5}$$

The velocity induced by the electrohydrodynamic flow decays more slowly compared to the migration velocity due to the DEP force [6,21], which is given by

$$U_{\mathrm{DEP}} = \frac{1}{h^4}\left(\frac{\varepsilon E_0^2 a^5}{\mu}\right)\left[\frac{3(1 + \lambda)}{8(2 + 3\lambda)}\left(\frac{1 - \mathrm{R}}{2 + \mathrm{R}}\right)^2\right]. \tag{6}$$

Note that Eqs. (5) and (6) are far-field descriptions of the drop velocity in the limit of no deformation and negligible surface-charge convection.

In this paper, we test these theoretical predictions using a combination of experiment and numerical simulations.

II. MATERIALS AND METHODS

A. Experiments

A polydimethylsiloxane (PDMS, hereafter referred to as silicone oil) drop is immersed in a castor oil medium, both obtained from Sigma-Aldrich. The material properties are summarized in Table I.

TABLE I. Material properties for the leaky dielectric drop (silicone oil) and medium (castor oil) used in this study.

Material	Density, ρ (kg/m^3)	Relative permittivity, ε_r	Conductivity, σ (pS/m)	Viscosity, μ (Pa s)	t_{EHD}, $\frac{\mu}{\varepsilon E_0^2}$ (s)	t_c, $\frac{\varepsilon}{\sigma}$ (s)
Silicone oil	961.08	1.70	1.2	0.047		12.54
Castor oil	958.46	2.0	45	0.66	0.25–2.0	0.39
	$\Delta\rho = 2.62$ kg/m^3	P = 0.85	R = 0.027	$\lambda = 0.07$		

The density of the fluids is measured directly from the weight of a known volume of the liquids. Viscosity values are measured with a TA Instruments Discovery HR-30 rheometer. Permittivity values are measured using a rheoimpedance spectroscopy stage and a 40 mm parallel plate for a Discovery HR-30 rheometer obtained from TA Instruments connected to a Keysight E4990A Impedance Analyzer. Conductivity values were measured in a previous work [22] and the reported values correspond to permittivity ratio P = 0.85, conductivity ratio R = 0.027, and viscosity ratio $\lambda = 0.07$. The material properties are validated by comparing the steady-state shape deformation of a silicone oil drop in castor oil with Taylor's small deformation theory [18] in the limit of weak electric fields; see Fig. 1. The deformation parameter $\mathcal{D}$ is used to quantify the drop's deviation from a spherical shape and is defined as

$$\mathcal{D} = \frac{l-b}{l+b}, \tag{7}$$

where l and b denote the drop's major axes parallel and perpendicular to the applied electric field, respectively.

The droplet dynamics in the electric field involves processes occurring on different time scales. Of particular interest is the time scale of the electrohydrodynamic flow $t_{\text{EHD}} = \mu/\varepsilon E_0^2$. The conduction of charges is dictated by the charge relaxation time $t_c = \varepsilon/\sigma$, while the viscocapillary time scale $t_\gamma = \mu a/\gamma$ governs the drop shape relaxation. The comparison of these time scales defines the

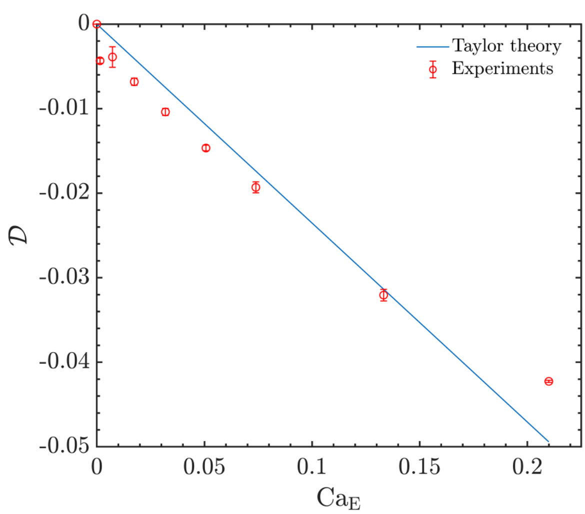

FIG. 1. Oblate drop deformation as a function of the electric capillary number. The red markers show the experimental results and the blue line is from Taylor's small deformation theory [18]. The error bar shows the standard deviation from three experiments. The droplet radius is $a = 1.8$ mm.

dimensionless parameters

$$\mathrm{Ca}_{\mathrm{E}} = \frac{t_\gamma}{t_{\mathrm{EHD}}} = \frac{\varepsilon\, a\, E_0^2}{\gamma}, \quad \mathrm{Re}_{\mathrm{E}} = \frac{t_c}{t_{\mathrm{EHD}}} = \frac{\varepsilon^2\, E_0^2}{\mu\, \sigma}. \tag{8}$$

The electric capillary number Ca_{E} measures the relative strength of electric forces against surface tension, while the electric Reynolds number Re_{E} determines the significance of surface charge convection relative to Ohmic conduction.

The silicone oil/castor oil system is commonly used in electrohydrodynamic studies due to the relatively small density difference between the two materials, with $\Delta\rho/\rho \sim O(10^{-3})$. This density difference results in drop migration due to buoyancy on a time scale that is significantly longer than the electrohydrodynamic time scale in our system, with $t_{\mathrm{EHD}}/t_b \sim O(10^{-2})$ at most. The buoyancy time scale, $t_b = \frac{3\mu}{2ag\Delta\rho}(\frac{2+3\lambda}{1+\lambda})$, is estimated from the Hadamard-Rybczynski settling velocity [23]. Finally, the inertial-viscous Reynolds number, $\mathrm{Re} = \rho a^2 \varepsilon E_0^2/\mu^2$, is estimated, using typical material properties and experimental electric field strengths, to be $\mathrm{Re} \sim O(10^{-3})$. Consequently, inertial effects are negligible in this system.

The experimental setup consists of a rectangular chamber formed by four glass plates mounted in a 3D-printed base. Two opposing sides (75 mm × 50 mm) are made from indium-tin oxide (ITO) coated glass (Delta Technologies), allowing the plates to serve as transparent electrodes. The other two plates (75 mm × 25 mm) are nonconductive, providing visual access to the experiment and create $d = 25$ mm spacing between the electrodes. A rectangular Teflon insert (thickness 12.7 mm) is placed at the base of the chamber, serving as the insulating wall. Attached to the ITO-coated glass are high-voltage wires connected to an Ultravolt 40A12-P4 high-voltage converter powered by an Agilent E646A dc power supply.

In the experiments, a constant dc voltage V is applied to generate a uniform electric field of strength $E_0 = V/d$. In this study, the strength of electric field is varied between 1.37 kV/cm and 3.8 kV/cm. The trajectories of the drop are recorded using a Thorlab DCU224M camera with Navitar Zoom 7000 lens collecting images at 15 frames per second.

The experiment is prepared by injecting a silicone oil drop of radius $a \sim 1.5$–2 mm into the chamber filled with castor oil. Due to the slight density mismatch in the materials (Table I), the drop slowly sediments towards the Teflon base. When it gets close to the base, at a distance h_0, the signal generator is switched on to apply the voltage, providing a constant dc electric field. The ensuing motion of the drop is monitored for approximately 30 s and saved as a video.

Figure 2 shows snapshots of a drop drifting away from the wall. The application of the electric field causes the drop to deform oblately, taking the appearance of an ellipse from the perspective of the camera. The droplet trajectories are calculated using MATLAB to track the position of the ellipse center as a function of time, creating a data set of the drop height relative to the wall: h (mm), as a function of time, t (s). Time $t = 0$ is defined as the frame in which the drop just begins to lift off from the wall.

B. Numerical simulations

This section presents the governing equations used in the numerical simulations, expressed in nondimensional form. The characteristic quantities used for nondimensionalization are length a, time $t_c = \varepsilon/\sigma$, velocity a/t_{EHD}, pressure εE_0^2, charge εE_0, and electric potential $a E_0$. All equations presented hereafter are expressed in these dimensionless terms. We consider a neutrally buoyant drop of leaky dielectric fluid occupying a volume V^-, immersed in a semi-infinite body of another leaky dielectric fluid V^+, positioned near a flat wall. The system is subject to a uniform electric field oriented parallel to the wall. Following the Taylor-Melcher leaky dielectric model [19], we assume that any free charge in the system is confined to the interface ∂V and the bulk of the fluids remains electroneutral. Consequently, the electric potential within the bulk is governed by Laplace's equation. The electric problem can be formulated in an integral form [25–27]. For every

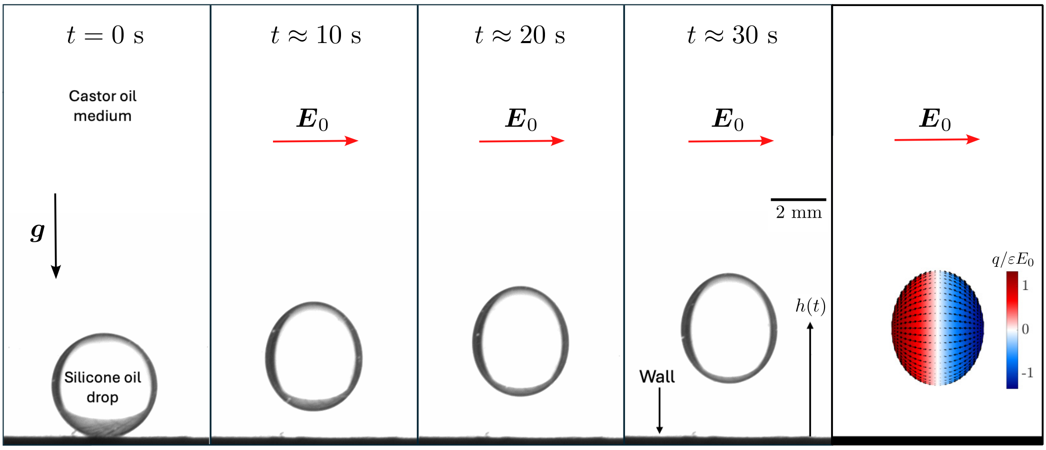

FIG. 2. Droplet migrating away from an insulating wall under an electric field applied parallel to the boundary. The figure shows experimental images (panels 1–4), see video [24], and a simulation result (last panel on the right) for a drop with (R, P, λ) = (0.027, 0.85, 0.07) migrating away from an insulating wall in an electric field, applied tangentially to the wall, corresponding to an electric capillary number $\mathrm{Ca_E} = 0.43$. The color on the drop from the numerical simulations represents the induced surface charge, while the overlaid vectors illustrate the interfacial velocity field.

$\boldsymbol{x}_0 \in V^{\pm},\ \partial V$,

$$\varphi(\boldsymbol{x}_0) = -\boldsymbol{x}_0 \cdot \boldsymbol{E}_0 - \int_{\partial V} \boldsymbol{n} \cdot [\![\nabla\varphi(\boldsymbol{x})]\!]\, \mathcal{G}^w(\boldsymbol{x}_0;\boldsymbol{x})\, ds(\boldsymbol{x}), \tag{9}$$

where $\mathcal{G}^w(\boldsymbol{x}_0;\boldsymbol{x}) = (4\pi r)^{-1} + (4\pi\tilde{r})^{-1}$ is the Green's function describing the electric potential due to a point charge near an insulating wall located at $x_w = 0$. Here, $\tilde{\boldsymbol{x}}_0$ is the mirror image of $\boldsymbol{x}_0$ with respect to the wall, with $\boldsymbol{r} = \boldsymbol{x}_0 - \boldsymbol{x},\ r = |\boldsymbol{r}|$ and $\tilde{\boldsymbol{r}} = \tilde{\boldsymbol{x}}_0 - \boldsymbol{x},\ \tilde{r} = |\tilde{\boldsymbol{r}}|$. The operator $[\![g]\!] := g^+ - g^-$ denotes the jump in any variable g across the interface ∂V. According to Gauss's law, the surface charge density is related to the jump in the normal electric field across the interface as $q(\boldsymbol{x}) = \boldsymbol{n} \cdot (\boldsymbol{E}^+ - \mathrm{P}\boldsymbol{E}^-)$, where $\boldsymbol{x} \in \partial V$. Taking the gradient of Eq. (9) with respect to $\boldsymbol{x}_0$ and considering the jump across the interface, we derive an integral equation for the jump in the normal electric field. For $\boldsymbol{x}_0 \in \partial V$,

$$\frac{1}{2}[\![E^n(\boldsymbol{x})]\!] = E_0^n(\boldsymbol{x}_0) - \fint_{\partial V} [\![E^n(\boldsymbol{x})]\!][\boldsymbol{n}(\boldsymbol{x}_0) \cdot \nabla_0 \mathcal{G}^w]\, ds(\boldsymbol{x}). \tag{10}$$

The surface charge evolves due to bulk Ohmic and convective surface currents, satisfying the conservation equation

$$\partial_t q + \boldsymbol{n} \cdot (\boldsymbol{E}^+ - \mathrm{R}\boldsymbol{E}^-) + \mathrm{Re_E}\nabla_s \cdot (q\boldsymbol{u}) = 0, \quad \boldsymbol{x} \in \partial V, \tag{11}$$

where $\nabla_s = (\boldsymbol{I} - \boldsymbol{nn}) \cdot \nabla$ denotes the surface gradient operator.

In the absence of inertial and buoyancy effects, the velocity and pressure fields are governed by the Stokes and continuity equations. The flow problem is then recast as a boundary integral equation [28,29]. For every $\boldsymbol{x}_0 \in \partial V$,

$$\boldsymbol{u}(\boldsymbol{x}_0) = -\mathcal{K}\int_{\partial V} [\![\boldsymbol{f}^{\mathrm{H}}(\boldsymbol{x})]\!] \cdot \boldsymbol{G}^w(\boldsymbol{x}_0;\boldsymbol{x})\, ds(\boldsymbol{x}) + (1-\lambda)\mathcal{K}\fint_{\partial V} \boldsymbol{u}(\boldsymbol{x}) \cdot \boldsymbol{T}^w(\boldsymbol{x}_0;\boldsymbol{x}) \cdot \boldsymbol{n}(\boldsymbol{x})\, ds(\boldsymbol{x}), \tag{12}$$

where $\mathcal{K} = 1/[4\pi(1+\lambda)]$. Here, $\boldsymbol{G}^w(\boldsymbol{x}_0;\boldsymbol{x})$ is Blake's Green's function for the flow due to a unit point force near a plane wall and $\boldsymbol{T}^w(\boldsymbol{x}_0;\boldsymbol{x})$ is the corresponding stress tensor [30,31].

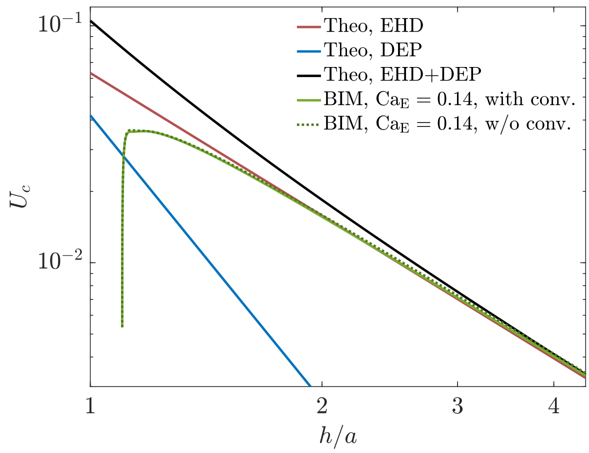

FIG. 3. Comparison between the migration velocity computed numerically and theoretically from Eqs. (5) and (6). Migration velocity as a function of distance from the wall for a drop with $(\mathrm{R},\ \mathrm{P},\ \lambda) = (0.027,\ 0.85,\ 0.07)$ and $(\mathrm{Ca_E},\ \mathrm{Re_E}) = (0.14,\ 0.19)$ with and without charge convection. Results from boundary integral simulations are compared with the theoretical predictions from Eqs. (5) and (6). The drop is initially positioned at $h_0/a = 1.1$ in the simulations.

The balance of external and internal forces at the interface is governed by

$$[\![\boldsymbol{f}^{\mathrm{H}}]\!] + [\![\boldsymbol{f}^{\mathrm{E}}]\!] = \mathrm{Ca}_{\mathrm{E}}^{-1}\,(\boldsymbol{\nabla}_s \cdot \boldsymbol{n})\,\boldsymbol{n}, \quad \boldsymbol{x} \in \partial V. \tag{13}$$

This dynamic boundary condition ensures that the jump in hydrodynamic and electric tractions is balanced by capillary forces, assuming uniform surface tension ($\boldsymbol{\nabla}_s \gamma = \boldsymbol{0}$). Hydrodynamic and electric tractions are expressed in terms of the Newtonian and Maxwell stress tensors, respectively:

$$[\![\boldsymbol{f}^{\mathrm{H}}]\!] = \boldsymbol{n} \cdot [(-p\boldsymbol{I} + (\boldsymbol{\nabla u} + \boldsymbol{\nabla u}^T))^+ - (-p\boldsymbol{I} + \lambda(\boldsymbol{\nabla u} + \boldsymbol{\nabla u}^T))^-], \tag{14}$$

$$[\![\boldsymbol{f}^{\mathrm{E}}]\!] = \boldsymbol{n} \cdot \left[\left(\boldsymbol{EE} - \tfrac{1}{2}E^2\boldsymbol{I}\right)^+ - \mathrm{P}\left(\boldsymbol{EE} - \tfrac{1}{2}E^2\boldsymbol{I}\right)^-\right]. \tag{15}$$

Finally, the drop's shape evolves according to the normal velocity at the interface:

$$\partial_t \boldsymbol{x} = \mathrm{Re}_{\mathrm{E}}(\boldsymbol{u} \cdot \boldsymbol{n})\boldsymbol{n}, \quad \boldsymbol{x} \in \partial V. \tag{16}$$

The velocity of the drop's center of volume, $\boldsymbol{U}_c$, is calculated as

$$\boldsymbol{U}_c(t) = \frac{1}{V_d}\int_{V^-} \boldsymbol{u}\, dv = \frac{1}{V_d}\int_{\partial V} \boldsymbol{x}\,(\boldsymbol{n} \cdot \boldsymbol{u})\, ds, \tag{17}$$

where V_d is the drop volume. In our system, the velocity is aligned with the x axis, such that $\boldsymbol{U}_c = U_c\,\boldsymbol{e}_x$.

We numerically solve Eqs. (10)–(13) and (16) using a spectral boundary integral solver developed for electrohydrodynamic flows in viscous drops [32,33]. Figure 2 compares snapshots of a drop migrating away from the wall in experiments and simulations, with good agreement between the two. Figure 3 provides a more precise validation of the numerical method. It illustrates the evolution of the droplet migration velocity upon application of the field obtained from simulations. After an initial transient, due to droplet deformation and polarization, the velocity approaches the theoretical result (5). We performed two sets of simulations: one that fully accounts for charge conservation as described in Eq. (11) and another in which the convective term is neglected. The results show that charge convection has little impact on the migration velocity. Consequently, charge convection is omitted in the simulations for the remainder of this study. At higher electric field strengths, however, the role of charge convection becomes more pronounced. For oblate drops with low viscosity ratios,

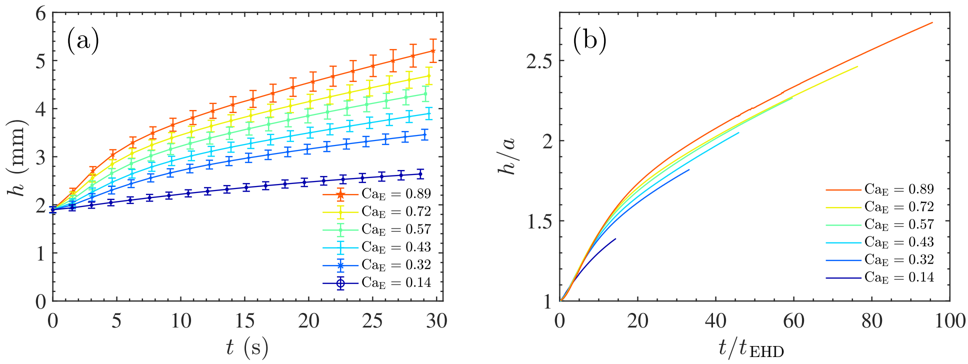

FIG. 4. Droplet drift away from an insulating wall. Droplet height above the wall as a function of time at increasing values of the electric field represented by the electric capillary number $\mathrm{Ca}_E = \varepsilon a E_0^2/\gamma$, for a droplet of radius $a = 1.90$ mm. The dimensional trajectories are shown in (a), where the lines and error bars show the average migration height and total error from three different experiments combined with the error due to optical distortion and contour detection, respectively. The nondimensionalized trajectories are shown in (b).

it is known that charge convection can generate steep charge gradients, leading to charge density shocks [32,34,35] resulting in equatorial streaming [36–38] or electrorotational instabilities [39–41]. In the experiments, however, the range of Ca_E corresponds to values of Re_E from 0.2 to 1.53, well below the conditions for such instabilities to occur.

III. RESULTS AND DISCUSSION

A. Oblate drops

Figure 4 shows the drift of the leaky dielectric drop away from the wall, demonstrating the existence of the migration phenomenon and indicating that the migration speed increases with capillary number (and therefore with electric field strength, $\mathrm{Ca}_E \sim E_0^2$). Figure 4(a) shows the dimensional trajectories, while the nondimensional trajectories are shown in Fig. 4(b).

In Figs. 5(a) and 5(b), the trajectories of two drop sizes $a = 1.46$ mm and 1.90 mm, respectively, from experiments, subject to electric fields from $E_0 = 1.37$ kV/cm to 3.8 kV/cm, are plotted as solid lines on a log-log scale, with the elevation h (distance between the drop center and the wall) and time t nondimensionalized by the drop radius a and by the electrohydrodynamic time $t_{\mathrm{EHD}} = \mu/\epsilon E_0^2$, respectively. The color indicates the value of the electric capillary number Ca_E, which varies from $\mathrm{Ca}_E = 0.1$ to 1. The cube of the initial position is subtracted from the cube of the distance from the wall and has been plotted as a function of time, which eliminates the dependence on the initial location. The EHD theory of Eq. (5) is plotted as a black dashed line. The long-term behavior of the experimental trajectories is well matched by the theory; however, the velocity in the near-wall region is overpredicted by Eq. (5)—likely due to near-wall effects not accounted for in the theory, including non-negligible contributions of higher-order images. The droplet trajectories computed from numerical simulations are also plotted as solid lines in Fig. 5(c), showing favorable agreement with both the theory and experiments. Experimental trajectories for $\mathrm{Ca}_E = 0.32$ and $\mathrm{Ca}_E = 0.89$ are also plotted as circular markers in Fig. 5(c) to demonstrate this agreement. The choice to plot this in a log-log scale was made for two reasons: (1) it more clearly highlights the long term power-law scaling and (2) it collapses the data for experiments in which the EHD time, which scales with E_0^2, varies over a wide range (from 0.25 s to 2 s). In the simulations, the drop is initially positioned at $h/a = 1.1$ with zero charge. Consequently, its early migration is primarily driven by DEP interactions at initial times. As charge accumulates on the drop's surface, EHD effects intensify, leading to increased migration velocities. During this transient regime, the distance from the wall does not follow the scaling behavior predicted by Eq. (5) or (6). Eventually,

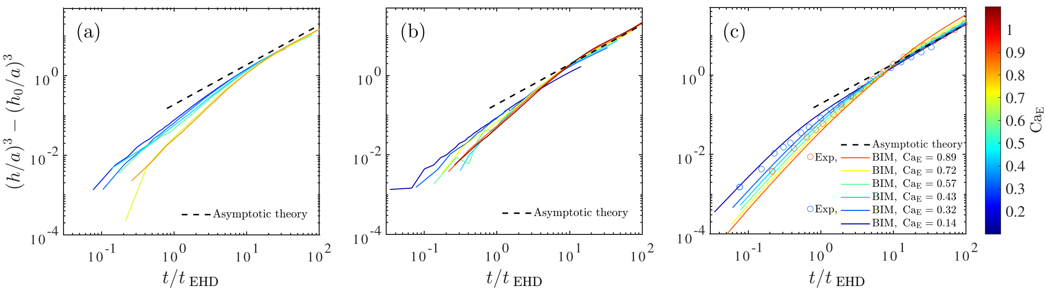

FIG. 5. Droplet height evolution. Experimental measurements of droplet elevation, normalized by the drop radius, plotted as a function of time, normalized by the electrohydrodynamic time, for drops of radius 1.46 mm and 1.90 mm, are shown in (a) and (b), respectively, as solid lines. The color of the trajectories denotes the value of the electric capillary number, which varies from approximately $\mathrm{Ca_E} = 0.1$ to 1, showing favorable agreement with Eq. (5). The theory predicts the scaling $(h/a)^3 \sim t/t_{\mathrm{EHD}}$ (black dashed line), emphasizing the dominance of EHD forcing in the far field. The (cube of the) initial height is subtracted from the ordinate to more clearly demonstrate this scaling. The results from boundary integral (BIM) simulations for a drop of radius 1.90 mm and different capillary numbers are plotted in (c) as solid lines and agree well with the experiments, plotted as circular markers for $\mathrm{Ca_E} = 0.32$ and $\mathrm{Ca_E} = 0.89$.

as the charge density approaches its steady distribution and the drop moves farther from the wall, EHD interactions dominate, and the distance from the wall exhibits the scaling predicted by Eq. (5).

The EHD flow, along with the streaming flow induced by drop migration, sweeps the charges accumulated on the droplet surface. The extent of the convection effect by the EHD flow is quantified by the electric Reynolds number, which is found to be $\mathrm{Re_E} \approx 0.2$ at the lower values of the electric capillary number, $\mathrm{Ca_E} = 0.14$. This regime, characterized by weak charge convection, is where our theory and simulations are expected to be most accurate. The charge convection due to the droplet translation is quantified as $\mathrm{Re}^*_{\mathrm{E}} = \varepsilon U_t/a\sigma$, where U_t is the droplet translation velocity from our experiments. In this case, we estimate $\mathrm{Re}^*_{\mathrm{E}} \sim O(10^{-2})$, indicating that charge convection due to the streaming flow around the translating drop is negligible in our system.

Figure 5 demonstrates favorable agreement with Eq. (5) at long times, which suggests negligible contribution from dielectrophoresis. The ratio of the two velocity contributions,

$$\frac{U_{\mathrm{DEP}}}{U_{\mathrm{EHD}}} = -\frac{10}{9}\frac{(1+\lambda)^2(1-\mathrm{R})^2}{(2+3\lambda)(\mathrm{R}-\mathrm{P})}\left(\frac{a}{h}\right)^2, \tag{18}$$

is, for the present leaky dielectric system, at most 0.66 at $h/a = 1$ (i.e., for a drop touching the wall) and is 0.1 at $h/a = 2.5$. However, note that for an electrohydrodynamic system with a smaller value of $(\mathrm{R/P} - 1)$ (the factor that sets the EHD flow strength) or a larger drop viscosity (and thereby a larger λ; silicone oil, for example, is available at a viscosity 200 times larger than that used here such that $\lambda \sim 14$), the dielectrophoretic force can become consequential in the near-wall migration behavior.

For a mobile interface (i.e., a fluid drop with $\lambda < \infty$), at distances sufficiently far away from the wall, EHD forcing will eventually overtake DEP forcing, due to the slower, $1/h^2$, decay of U_{EHD}. For a solid "drop" (particle), $\lambda \to \infty$ and the EHD flow is supressed. Accordingly, there is no EHD-induced migration and the migration is purely due to dielectrophoresis. It is worth emphasizing that these equations are far-field descriptions of the flow field—higher-order descriptions of the flow singularity are unaccounted for, though these contributions are expected to be significant close to the wall $h/a \sim O(1)$. Despite these approximations, Fig. 5 demonstrates the existence of the electrohydrodynamic migration phenomenon and its domination over the dielectrophoretic migration in leaky dielectric systems.

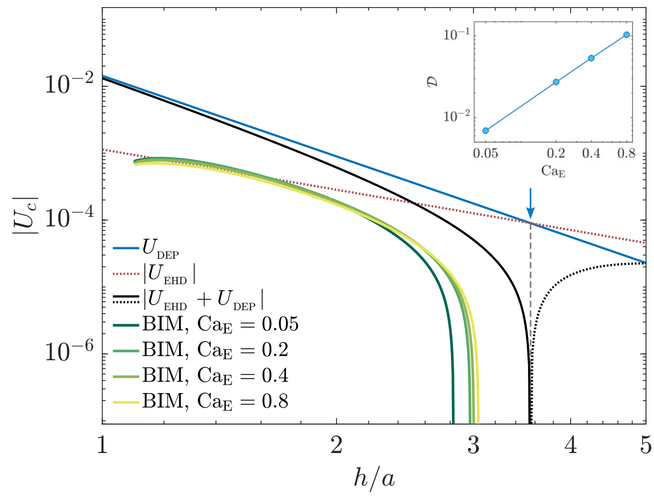

FIG. 6. Antagonistic EHD and DEP interactions can result in a hovering drop. Migration velocity as a function of distance from the wall in a drop with $(\mathrm{R},\ \mathrm{P},\ \lambda) = (0.25,\ 0.063,\ 10)$ at various electric capillary numbers, compared with theoretical predictions from Eqs. (5) and (6). In all simulations, the drop is initially positioned at $h_0/a = 1.1$ from the wall and its trajectory is subsequently computed. Solid lines indicate positive migration velocities (away from the wall), while dotted lines indicate negative velocities (towards the wall). The inset shows the deformation parameter at the hovering point in each case. The arrow indicates the hovering height determined by the theory.

B. Prolate drops

We extend our analysis to prolate drops, characterized by $\mathrm{R}/\mathrm{P} > 1$. In this regime, EHD and DEP effects act in opposition, potentially leading to a steady hovering state where the two forces balance. However, prolate systems are harder to realize experimentally, especially since they are unstable and prone to breakup at high electric field strengths needed to induce significant migration. Therefore, our analysis in this section relies on asymptotic theory and numerical simulations. Figure 6 presents the magnitude of the migration velocity as a function of wall separation for a prolate drop. Solid lines indicate motion away from the wall, while dotted lines denote motion toward it. As described by Eqs. (5) and (6), DEP and EHD interactions counteract each other: short-range DEP repulsion and long-range EHD attraction establish a steady hovering state at a predicted equilibrium distance of $h/a \approx 3.5$ from the wall. We note that the hovering position observed in numerical simulations deviates from theoretical predictions. Additionally, for a viscosity ratio of $\lambda = 1$, no hovering state is observed and the drop instead migrates toward the wall. These discrepancies arise from near-wall hydrodynamic effects, which are not accounted for in the asymptotic theory. Furthermore, increasing the electric capillary number $\mathrm{Ca_E}$ shifts the hovering point further from the wall.

IV. CONCLUSIONS AND OUTLOOK

In this paper, we have investigated the dynamics of oblate droplets ($\mathrm{R}/\mathrm{P} < 1$), for which the electrohydrodynamic flow induces migration with velocity $U_{\mathrm{EHD}} \sim 1/h^2$ away from the wall, considerably stronger than the dielectrophoretic attraction to the wall ($U_{\mathrm{DEP}} \sim 1/h^4$), leading to a pronounced lift. This work highlights the importance of boundaries on droplet behavior in electric fields and develops a simple theory describing the migration velocity in terms of the leading flow singularity, a stresslet. Since boundaries are always present in applications like microfluidics, droplet migration driven by EHD flow may play an important role. Our paper quantifies this effect and shows that the drift can be accurately predicted using asymptotic theory, which estimates droplet migration due to the stresslet-image-induced flow—a result that was not obvious *a priori*.

ACKNOWLEDGMENTS

The authors would like to thank Dr. P. Salipante for generously sharing his expertise and M. Brucks, X. Wan, L. Pham, and Dr. J. J. Richards for their help with measuring the fluid viscosities and permittivities. This research was supported by National Science Foundation Award No. CBET-2126498 (P.M.V. and Sen).

DATA AVAILABILITY

The data that support the findings of this article are openly available [42].

APPENDIX: STOKES GREEN'S FUNCTIONS FOR THE FLOW NEAR A PLANE WALL

In their seminal work, Blake and Chwang derived the Stokes Green's function associated with a point force near a plane wall [29–31]. The velocity tensor near a wall located at $x = x_w$ is given by

$$G^w_{ij}(\boldsymbol{x}_0;\boldsymbol{x}) = G^{FS}_{ij}(\boldsymbol{r}) - G^{FS}_{ij}(\tilde{\boldsymbol{r}}) + 2\,d_0^2\,D_{ij}(\tilde{\boldsymbol{r}}) - 2\,d_0\,Q_{ij}(\tilde{\boldsymbol{r}}), \tag{A1}$$

where $d_0 = x_0 - x_w$ is the distance of the point force from the wall. Here, $\tilde{\boldsymbol{x}}_0$ denotes the mirror image of $\boldsymbol{x}_0$ with respect to the wall, with $\boldsymbol{r} = \boldsymbol{x}_0 - \boldsymbol{x},\ r = |\boldsymbol{r}|$ and $\tilde{\boldsymbol{r}} = \tilde{\boldsymbol{x}}_0 - \boldsymbol{x},\ \tilde{r} = |\tilde{\boldsymbol{r}}|$. The first two terms on the right-hand side of (A1) represent the primary and image Stokeslets in free space. The terms D_{ij} and Q_{ij} correspond to the potential dipole and point force doublet, respectively:

$$G^{FS}_{ij}(\boldsymbol{r}) = \frac{\delta_{ij}}{r} + \frac{r_i\,r_j}{r^3}, \tag{A2}$$

$$D_{ij}(\boldsymbol{r}) = \pm\left(\frac{\delta_{ij}}{r^3} - 3\frac{r_i\,r_j}{r^5}\right), \tag{A3}$$

$$Q_{ij}(\boldsymbol{r}) = r_1 D_{ij}(\boldsymbol{r}) \pm \left(\frac{\delta_{j1}\,r_i - \delta_{i1}\,r_j}{r^3}\right). \tag{A4}$$

The minus sign corresponds to $j = 1$ (x direction) and the positive sign applies to $j = 2, 3$ (y and z directions).

The associated stress tensor for this Green's function is

$$T^w_{ijk}(\boldsymbol{x}_0;\boldsymbol{x}) = T^{FS}_{ijk}(\boldsymbol{r}) - T^{FS}_{ijk}(\tilde{\boldsymbol{r}}) + 2\,d_0^2\,T^D_{ijk}(\tilde{\boldsymbol{r}}) - 2\,d_0\,T^Q_{ijk}(\tilde{\boldsymbol{r}}), \tag{A5}$$

where

$$T^{FS}_{ijk}(\boldsymbol{r}) = -6\frac{r_i\,r_j\,r_k}{r^5}, \tag{A6}$$

$$T^D_{ij}(\boldsymbol{r}) = \pm 6\left(-\frac{\delta_{ij}r_k + \delta_{ik}r_j + \delta_{kj}r_i}{r^5} + 5\frac{r_i\,r_j\,r_k}{r^7}\right), \tag{A7}$$

$$T^Q_{ij}(\boldsymbol{r}) = r_1 T^D_{ijk}(\boldsymbol{r}) \pm 6\left(\frac{\delta_{ik}\,r_j\,r_1 - \delta_{j1}\,r_i\,r_k}{r^5}\right). \tag{A8}$$

Similarly, the minus sign corresponds to $j = 1$ and the positive sign applies to $j = 2, 3$.

---

[1] O. D. Velev, S. Gangwal, and D. N. Petsev, Particle-localized AC and DC manipulation and electrokinetics, Annu. Rep. Prog. Chem., Sect. C: Phys. Chem. **105**, 213 (2009).

[2] A. Boymelgreen, J. Schiffbauer, B. Khusid, and G. Yossifon, Synthetic electrically driven colloids: A platform for understanding collective behavior in soft matter, Curr. Opin. Colloid Interface Sci. **60**, 101603 (2022).
[3] N. M. Diwakar, G. Kunti, T. Miloh, G. Yossifon, and O. D. Velev, AC electrohydrodynamic propulsion and rotation of active particles of engineered shape and asymmetry, Curr. Opin. Colloid Interface Sci. **59**, 101586 (2022).
[4] A. A. Harraq, B. D. Choudhury, and B. Bharti, Field-induced assembly and propulsion of colloids, Langmuir **38**, 3001 (2022).
[5] A. M. Gañán-Calvo, J. M. López-Herrera, M. A. Herrada, A. Ramos, and J. M. Montanero, Review on the physics of electrospray: From electrokinetics to the operating conditions of single and coaxial Taylor cone-jets, and AC electrospray, J. Aerosol Sci. **125**, 32 (2018).
[6] P. M. Vlahovska, Electrohydrodynamics of drops and vesicles, Annu. Rev. Fluid Mech. **51**, 305 (2019).
[7] C. D. McCaig, B. Song, and A. M. Rajnicek, Electrical dimensions in cell science, J. Cell Sci. **122**, 4267 (2009).
[8] M. A. Messerli and D. M. Graham, Extracellular electrical fields direct wound healing and regeneration, Biol. Bull. **221**, 79 (2011).
[9] A. Agrawal, J. F. Douglas, M. Tirrell, and A. Karim, Manipulation of coacervate droplets with an electric field, Proc. Natl. Acad. Sci. USA **119**, e2203483119 (2022).
[10] R. Dimova, K. A. Riske, S. Aranda, N. Bezlyepkina, R. L. Knorr, and R. Lipowsky, Giant vesicles in electric fields, Soft Matter **3**, 817 (2007).
[11] M. Aleksanyan, H. A. Faizi, M. A. Kirmpaki, P. M. Vlahovska, K. A. Riske, and R. Dimova, Assessing membrane material properties from the response of giant unilamellar vesicles to electric fields, Adv. Phys.: X **8**, 2125342 (2023).
[12] T. B. Jones, *Electromechanics of Particles* (Cambridge University Press, New York, 1995).
[13] E. Yariv, "Force-free" electrophoresis? Phys. Fluids **18**, 031702 (2006).
[14] M. S. Kilic and M. Z. Bazant, Induced-charge electrophoresis near a wall, Electrophoresis **32**, 614 (2011).
[15] Z. Wang, M. J. Miksis, and P. M. Vlahovska, Particle-surface interactions in a uniform electric field, Phys. Rev. E **106**, 034607 (2022).
[16] Z. Wang, M. J. Miksis, and P. M. Vlahovska, Electrostatic force on a spherical particle confined between two planar surfaces, Soft Matter **19**, 7663 (2023).
[17] H. Zhao and H. H. Bau, On the effect of induced electro-osmosis on a cylindrical particle next to a surface, Langmuir **23**, 4053 (2007).
[18] G. I. Taylor, Studies in electrohydrodynamics. I. Circulation produced in a drop by an electric field, Proc. R. Soc. A **291**, 159 (1966).
[19] J. R. Melcher and G. I. Taylor, Electrohydrodynamics: a review of role of interfacial shear stress, Annu. Rev. Fluid Mech. **1**, 111 (1969).
[20] J. R. Smart and D. T. Leighton, Jr., Measurement of the drift of a droplet due to the presence of a plane, Phys. Fluids A **3**, 21 (1991).
[21] C. Sorgentone, J. I. Kach, A. S. Khair, L. M. Walker, and P. M. Vlahovska, Numerical and asymptotic analysis of the three-dimensional electrohydrodynamic interactions of drop pairs, J. Fluid Mech. **914**, A24 (2021).
[22] P. F. Salipante and P. M. Vlahovska, Electrohydrodynamics of drops in strong uniform dc electric fields, Phys. Fluids **22**, 112110 (2010).
[23] G. K. Batchelor, *An Introduction to Fluid Dynamics* (Cambridge University Press, Cambridge, UK, 2000).
[24] See Supplemental Material at http://link.aps.org/supplemental/10.1103/l8pb-9qxk for video of the experiment.
[25] J. D. Sherwood, Breakup of fluid droplets in electric and magnetic fields, J. Fluid Mech. **188**, 133 (1988).
[26] J. C. Baygents, N. J. Rivette, and H. A. Stone, Electrohydrodynamic deformation and interaction of drop pairs, J. Fluid Mech. **368**, 359 (1998).
[27] E. Lac and G. M. Homsy, Axisymmetric deformation and stability of a viscous drop in a steady electric field, J. Fluid Mech. **590**, 239 (2007).

[28] J. M. Rallison and A. Acrivos, A numerical study of the deformation and burst of a viscous drop in an extensional flow, J. Fluid Mech. **89**, 191 (1978).

[29] C. Pozrikidis, *Boundary Integral and Singularity Methods for Linearized Viscous Flow* (Cambridge University Press, Cambridge, UK, 1992).

[30] J. R. Blake, A note on the image system for a stokeslet in a no-slip boundary, Math. Proc. Cambridge Philos. Soc. **70**, 303 (1971).

[31] J. R. Blake and A. T. Chwang, Fundamental singularities of viscous flow. Part I: The image systems in the vicinity of a stationary no-slip boundary, J. Eng. Math. **8**, 23 (1974).

[32] M. Firouznia, S. H. Bryngelson, and D. Saintillan, A spectral boundary integral method for simulating electrohydrodynamic flows in viscous drops, J. Comput. Phys. **489**, 112248 (2023).

[33] M. Firouznia, S. H. Bryngelson, and D. Saintillan, Spectral boundary integral solver for electrohydrodynamic flows in viscous drops, https://github.com/mfirouzn/EHD_Drop_3D.

[34] G. G. Peng, R. Brandão, E. Yariv, and O. Schnitzer, Equatorial blowup and polar caps in drop electrohydrodynamics, Phys. Rev. Fluids **9**, 083701 (2024).

[35] J. A. Lanauze, L. M. Walker, and A. S. Khair, Nonlinear electrohydrodynamics of slightly deformed oblate drops, J. Fluid Mech. **774**, 245 (2015).

[36] Q. Brosseau and P. M. Vlahovska, Streaming from the equator of a drop in an external electric field, Phys. Rev. Lett. **119**, 034501 (2017).

[37] B. W. Wagoner, P. M. Vlahovska, M. T. Harris, and O. A. Basaran, Electric field induced transitions from spherical to discocyte and lens shaped drops, J. Fluid Mech. **904**, R4 (2020).

[38] B. W. Wagoner, P. M. Vlahovska, M. T. Harris, and O. A. Basaran, Electrohydrodynamics of lenticular drops and equatorial streaming, J. Fluid Mech. **925**, A36 (2021).

[39] P. F. Salipante, Electrohydrodynamics of drops in strong fields, Master's thesis, Dartmouth College, 2009.

[40] M. Ouriemi and P. M. Vlahovska, Electrohydrodynamics of particle-covered drops, J. Fluid Mech. **751**, 106 (2014).

[41] P. M. Vlahovska, Electrohydrodynamic instabilities of viscous drops, Phys. Rev. Fluids **1**, 060504 (2016).

[42] P. Vlahovska, Electrohydrodynamic drift of a drop away from an insulating wall: experimental data, https://doi.org/10.21985/n2-3nh6-3754.